Photoacoustics 20 (2020) 100201

Contents lists available at ScienceDirect

Photoacoustics

journal homepage: www.elsevier.com/locate/pacs

Research article

Photoacoustic imaging biomarkers for monitoring biophysical changes during nanobubble-mediated radiation treatment

Eno Hysi [a,b], Muhannad N. Fadhel [a,b,1], Yanjie Wang [a,b,1], Joseph A. Sebastian [a,b], Anoja Giles [c,d], Gregory J. Czarnota [c,d,e,f], Agata A. Exner [g,h], Michael C. Kolios [a,b,*]

[a] Department of Physics, Ryerson University, Toronto, Canada
[b] Insitute for Biomedical Engineering, Science and Technology, St. Michael's Hospital, Toronto, Canada
[c] Deparment of Radiation Oncology, Sunnybrook Health Sciences Center, Toronto, Canada
[d] Physical Sciences, Sunnybrook Research Institute, Toronto, Canada
[e] Deparment of Medical Biophysics, University of Toronto, Canada
[f] Department of Radiation Oncology, University of Toronto, Canada
[g] Department of Radiology, Case Western Reserve University, Cleveland, United States
[h] Department of Biomedical Engineering, Case Western Reserve University, Cleveland, United States

ARTICLE INFO

Keywords:
Nanobubbles
Microbubbles
Radiation therapy
Photoacoustic imaging
Vascular disruption

ABSTRACT

The development of novel anticancer therapies warrants the parallel development of biomarkers that can quantify their effectiveness. Photoacoustic imaging has the potential to measure changes in tumor vasculature during treatment. Establishing the accuracy of imaging biomarkers requires direct comparisons with gold histological standards. In this work, we explore whether a new class of submicron, vascular disrupting, ultrasonically stimulated nanobubbles enhance radiation therapy. *In vivo* experiments were conducted on mice bearing prostate cancer tumors. Combined nanobubble plus radiation treatments were compared against conventional microbubbles and radiation alone (single 8 Gy fraction). Acoustic resolution photoacoustic imaging was used to monitor the effects of the treatments 2- and 24-hs post-administration. Histological examination provided metrics of tumor vascularity and tumoral cell death, both of which were compared to photoacoustic-derived biomarkers. Photoacoustic metrics of oxygen saturation reveal a 20 % decrease in oxygenation within 24 h post-treatment. The spectral slope metric could separate the response of the nanobubble treatments from the microbubble counterparts. This study shows that histopathological assessment correlated well with photoacoustic biomarkers of treatment response.

1. Introduction

Despite the standardization of treatments such as surgery, chemotherapy and radiation therapy, overall cancer survival rates remain modest [1,2]. A deeper understanding of cancer causation and progression has driven the development of molecularly targeted drugs. These have lead to personalized, precision treatments that rely on individualized drug administration based on prognostic and predictive markers of response [3]. The ultimate hope is that such a personalized strategy in cancer therapy will replace the "one-size-fits-all" conventional approach, increasing overall survival rates [4]. This however remains a monumental task because the selection of the right treatment is a complex decision based on continuously changing molecular diagnostics and rapidly evolving biomedical literature [5].

Equally important to the developments of new drugs or experimental therapies is their assessment with inexpensive and readily available means, which can expedite their clinical translation [6]. A prime example of a successful biomarker-driven personalized cancer therapy is the development of trastuzumab for human epidermal growth factor 2 (HER2)-positive breast cancer [7]. However, the molecular heterogeneity of tumors can also lead to individualized and dynamic treatment-induced changes in tumor morphology and structure [8]. Unfortunately, current treatment efficacy assessment approaches might not be suitable for handling the complexities of personalized cancer treatments [8]. Studying the structural and functional markers of treatment response is thus imperative for providing fast and reliable

* Corresponding author at: Department of Physics, Ryerson University, 350 Victoria Street, Toronto, Ontario, M5B 2K3, Canada.
E-mail address: mkolios@ryerson.ca (M.C. Kolios).
[1] These authors contributed equally to this work.

https://doi.org/10.1016/j.pacs.2020.100201
Received 3 April 2020; Received in revised form 24 June 2020; Accepted 22 July 2020
Available online 25 July 2020
2213-5979/© 2020 The Author(s). Published by Elsevier GmbH. This is an open access article under the CC BY-NC-ND license (http://creativecommons.org/licenses/by-nc-nd/4.0/).

feedback on treatment efficacy [5].

Photoacoustic (PA) imaging is a relatively new modality that combines ultrasound (US) resolution with optical contrast. The optical absorption of pulsed laser light generates mechanical sound waves from the thermoelastic expansion of endogenous tissue chromophores [9]. In PA imaging, the strength of the signal depends on the tissue chromophore identity and concentration. As such, PA imaging has contributed to breast cancer diagnosis, mapping neuronal functional connectivity, quantifying pharmacokinetics of novel drugs and detecting the presence of malaria [10–13].

While a lot of strides have been made in the diagnostic realm [14–17], PA imaging applications in cancer treatment monitoring are still in their infancy. A handful of pre-clinical studies have illustrated the potential of PA imaging for the early monitoring of cancer therapies by mapping the tumor oxygenation changes post-treatment through measurements of oxygen saturation [18–22]. The clinical translation of PA imaging in cancer treatment monitoring warrants the development of non-invasive biomarkers whose detection and quantitative measurement is accurate, reproducible and feasible over time [3]. Just like for the US radiofrequency (RF) signals in quantitative ultrasound spectroscopy [23,24], the frequencies of the PA signals carry information on the structure (size, shape and orientation) of the underlying absorber [25–28]. In utilizing the frequency information of the PA RF signals, acoustic resolution PA imaging has the potential to probe non-resolvable optical absorbers and thus provide new PA biomarkers that can be linked to the success or failure of the therapy being evaluated.

In this study, we investigate for the first time the therapeutic application of ultrasonically activated nanobubbles (NBs) for enhancing radiation therapy. Ultra-stable NBs (100−300 nm diameter) are a new class of US contrast agents with contrast-enhancing capabilities comparable to conventional microbubbles (MBs, 1−10 μm diameter) [29–32]. The size range makes MBs ideal vascular disrupting agents. Under US stimulation, they can cause increased vascular permeability for amplifying tumoral drug release [33], inducing thrombolysis of blood clots [34] and open the blood brain barrier [35]. In contrast, NBs have been shown to remain echogenic at the clinical frequency range (3−12 MHz) [36] while being able to exit tumor vasculature due to the enhanced permeability and retention effect [37]. Unlike conventional MBs that remain intravascular, NBs can in principle directly target tumoral cells, thus having the potential to become multifunctional theranostic agents. The prolonged *in vivo* stability has allowed NBs to be used to open the blood brain barrier [29], enhance contrast in ovarian cancer [38] and increase chemotherapy uptake [30].

The ultrasonic stimulation of conventional MBs has been shown to enhance radiation therapy [39–41]. This combination treatment synergistically damages the endothelial lining of tumor blood vessels in addition to causing radiation-induced damage of cancer cells *in vivo*. However, a limitation of any MB-based treatments remains their limited *in vivo* stability [42] which reduces their circulation time and usability [32]. NB-enhancement of radiation therapy has the potential to further maximize the tumoral cell death through their extravascular effect. Histopathological examinations post-treatment have provided insights into the biophysical mechanism of MB treatments [41]. The damage caused to the vascular endothelium through mechanical perturbations and the production of reactive oxygen species can lead to secondary tumor cell death and vascular collapse. Here we investigate whether PA imaging biomarkers can quantify the vascular damage induced by ultrasound excitations of NBs combined with radiation, and if these biomarkers can be used to monitor treatment efficacy.

2. Materials and methods

2.1. Animal model and tumor growth

Severe combined immuno-deficient (SCID) male mice (Charles River Laboratories International, Wilmington, MA, USA) were inoculated with 10^6 human prostate cancer cells (PC3, American Type Culture Collection, Manassas, VA, USA) in order to grow xenograft tumors in the right, upper hind leg of each mouse (n = 58). Tumors were grown to 8–10 mm in maximum diameter for approximately 4–6 weeks. Following treatments, all animals were euthanized by cervical dislocation under anesthesia after 24 h in order to histologically assess the morphological changes to the tumor cells and blood vessels. The animal studies were approved by the Sunnybrook Research Institute Animal Ethics Committee and conformed to the Canadian Council on Animal Care guidelines.

2.2. Treatment groups

A total of 58 mice were divided into six treatment groups as summarized in Table 1.

2.3. Ultrasound-activated microbubble and nanobubble treatments

2.3.1. Microbubble preparations and injections

Commercially available Definity (Lantheus Medical Imaging, N. Billerica, MA, US) MBs (~3 μm mean diameter) were activated using the Lantheus Vialmix mechanical shaker device (45 s at 3000 rpm). An intravenous tail vein injection of a MB bolus (1.2×10^{10} MBs/mL) was administered to each mouse 5 min prior to the ultrasound activation.

2.3.2. Nanobubble preparations and injections

NBs were prepared using a previously established protocol [32]. The NBs consisted of a lipid shell and an octafluoropropane (C_3F_8, Electronic Fluorocarbons LLC, Hatfield, PA, USA) gas. The NB consisted of the following mixture of lipids (Avanti Polar Lipids, Inc.):

- 1,2-dipalmitoyl-sn-glycero-3-phosphoethanolamine
- 1,2-dibehenoyl-sn-glycero-3-phosphocholine
- 1,2-distearoyl-sn-glycero-3-phosphoethanolamine-*N*-[methoxy (polyethylene glycol)-2000]
- 1,2-dipalmitoyl-sn-glycero-3-phosphate

The lipid mixture with a 2:6:1:2 ratio was dissolved in propylene glycol and glycerol in Phosphate Buffered Saline (PBS) solution. The air present in the lipid-PBS solution was replaced by C_3F_8 prior to mechanically agitating the lipid-gas solution for 45 s using the Lantheus Vialmix in order to generate a mixture of MBs and NBs. In order to isolate the NBs from the mixture foam and the MB solution, centrifugation was performed at 50 *g* for 5 min. The NB solution was retrieved with the headspace vial inverted and by using a 21 G needle withdrawing from a fixed distance of 5 mm from the bottom of the vial.

The size and concentration of the resulting NB solution were assessed using resonant mass measurement (Archimedes®, Malvern Panalytical, Westborough, MA, USA) [31]. This device was equipped with a nanosensor which can measure particle sizes between 50 and 2000 nm. The NB solution was diluted by a factor of 1000 (v/v) in PBS prior to measurements. A size distribution representative of the NB formulation used in this study is shown in Fig. S1. The average diameter of the NB was measured to be 205 ± 97 nm. NBs were injected 5 min prior to ultrasound activation with a tail vain injection concentration of 1×10^{11}

Table 1
Experimental treatment groups for the MB and NB experiments.

Treatment group (abbreviation)	Number of animals
Untreated control (0 Gy)	14
Radiation only, 8 Gy, single fraction (8 Gy)	14
Microbubbles + Ultrasound (MB + US)	8
Nanobubbles + Ultrasound (NB + US)	5
Microbubbles + Ultrasound + Radiation (NB + US+8 Gy)	12
Nanobubbles + Ultrasound + Radiation (NB + US+8 Gy)	5

NBs/mL.

2.3.3. Low frequency ultrasound activation

Following the MB or NB bolus injections, 500 kHz frequency US treatments were administered 5 min post-injection. Fig. 1 shows a schematic of the treatment and imaging setups used to expose the MB and NB post-injection. The mice were secured onto a mounting platform with the lower half of the mouse and the tumor immersed in a degassed water bath kept at 37 °C (Fig. 1A). The platform was mounted coaxially to a therapeutic ultrasonic transducer such that the tumor was centered within the focus of the transducer through a micro-positioning system.

The low frequency ultrasonic activation of the MBs and NBs was generated using a 500 kHz focused transducer (Valpey Fisher Inc., Hopkinton, MA, USA) [39–41]. The transducer had a diameter of 28.7 mm, a focal depth of 85 mm, peak negative pressure of 570 kPa, a -6 dB beam width of 31 mm and a depth of field greater than 20 mm. It was connected to a PC-controlled digital acquisition system (Agilent Technologies Inc., Monroe, NY, USA) which controls a waveform generator (Tektronix Inc., Beaverton, OR, USA), a power amplifier and receiver (Ritec Inc., Warwick, RI, USA) using the setup previously described [43].

Following tail vein injection, bubbles were allowed to circulate for 5 min before ultrasonic activation. The ultrasonic activation treatment was administered for a total time of 5 min using 16 cycle tone bursts of 500 kHz frequency with a pulse repetition frequency of 3 kHz. This resulted in a duty cycle of 0.24 % or 720 ms of beam-on treatment time. This low duty cycle was designed to avoid any bioeffects potentially rising from ultrasound heating. It was previously estimated that for this system the transducer spatial peak temporal peak intensity was 22.4 W/cm^2 and the spatial peak temporal average intensity was 0.054 W/cm^2 [43]. The -3 dB beam width was determined to be 15.6 mm, ensuring that the entire tumor volume (diameter 8−10 mm) is consistently exposed to the ultrasound pulse.

2.4. Radiation treatments

Following the MB or NB treatments, a single dose of 8 Gy X-ray radiation was delivered through a 160 kVp small animal irradiator (Faxitron Bioptics, LLC, Tucson, AZ, USA). The dose was delivered at a rate of 200 cGy/min for a total of exactly 4 min, three hours following ultrasound treatments to maximize the degree of tumor cellular death [41]. The mouse was shielded with a lead sheet and a circular cutout in the hind leg enabled the irradiation of only the tumor.

2.4.1. Delayed tumor growth investigations

Another cohort of mice (n = 19) bearing subcutaneous PC3 tumors were treated either with a single dose of 8 Gy (n = 5), NB + US (n = 5), NB + US+8 Gy (n = 4) or were left untreated (n = 5). Instead of sacrificing at the 24 -h time point, the mice were followed longitudinally post-treatment for monitoring the growth delay effects of each treatment. The tumor size was measured *via* standard caliper measurements every 3–5 days for 30 days post-treatment.

2.5. Photoacoustic imaging and biomarkers

2.5.1. Imaging setup

Fig. 1B shows the positioning setup for performing PA imaging on the hind leg PC3 tumors of SCID mice. The VevoLAZR small animal PA imaging system (Fujifilm-VisualSonics, Toronto, Canada) was used to perform three-dimensional (3D) volume of the tumors. A 21 MHz linear array probe with 256 active transducer elements (LZ 250) was coupled to an Nd:YAG laser operating through an optical parametric oscillator in the 680−970 nm range [44]. The laser light (30 mJ/pulse, 20 Hz pulse repetition frequency, 6 ns pulse length) was delivered through a pair of optical fibers terminating in two rectangular strips located at a 30° angle on both sides of the acoustic aperture. Co-registered US and PA images were acquired at a rate of 5 frames/second at 750 nm and 850 nm. Each mouse was anesthetized using isoflurane (1.5 %) to immobilize them during imaging (Fig. 1B). The mice were imaged in the prone position in order to fully expose their hind leg tumor. Their core temperature was kept physiological with the help of an external heating lamp and a heated platform. The center of the tumor was positioned at the focus of the US/PA transducer (11 mm) and clear ultrasonic gel was used at provide acoustic coupling. The probe was scanned from the proximal towards the distal end of the tumor in 80 μm steps. At every step, a two-dimensional (2D), co-registered US and PA image was acquired for both imaging wavelengths at pre-treatment, 2 h and 24 h post-treatment.

2.5.2. Vessel oxygenation biomarkers

Fig. 2 shows a schematic overview of the PA biomarkers that were used in this work to examine the impact that ultrasound-simulated MB and NB treatments in combination with radiation have on the tumor viability and its blood vessels. Upon the administration of the MB or NB/

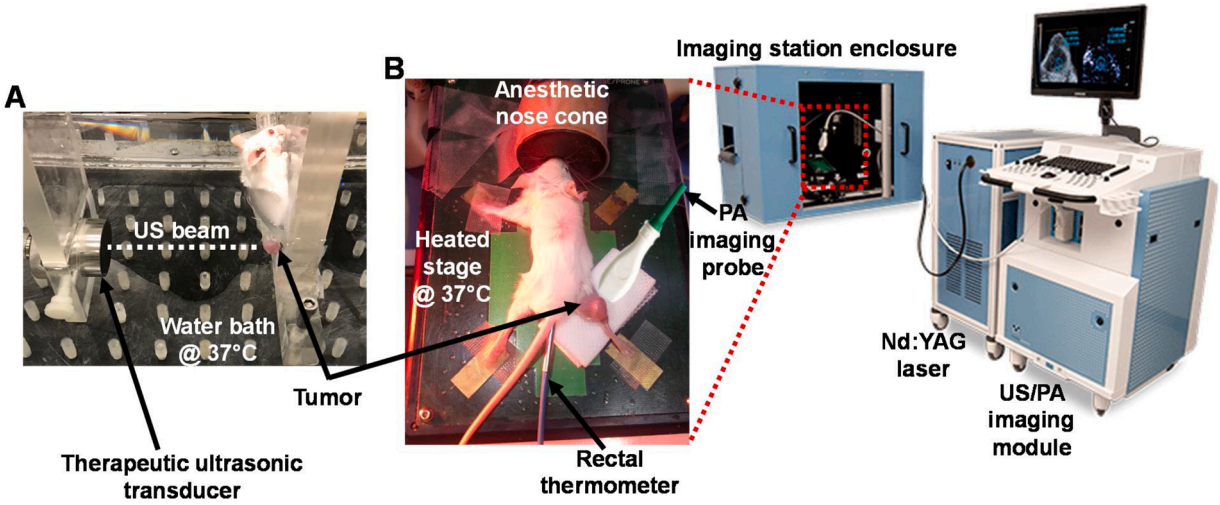

Fig. 1. Ultrasonic treatment and PA imaging setups.
(**A**) Ultrasonic bubble activation setup. The tumor is positioned at the focus of the therapeutic ultrasonic transducer. (**B**) PA imaging platform illustrating the prone imaging position of the mouse during imaging. The mice are kept at physiological temperature through a heated stage and a heating lamp. Acoustic coupling is achieved *via* clear ultrasonic gel.

radiation treatments, two-wavelength ($\lambda_1 = 750$ nm and $\lambda_2 = 850$ nm) PA images were acquired at each scanning location in the tumor. The oxygen saturation (sO_2) and the total hemoglobin (HbT) content present within the vessels were calculated by assuming that deoxy (Hb) and oxy (HbO) hemoglobin are the dominant absorbers inside tumor blood vessels [45]. At every 2D tumor slice, the sO_2 and HbT are calculated by:

$$sO_2 = \frac{[HbO]}{[HbO]+[Hb]} = \frac{\mu_a^{\lambda_2}\varepsilon_{Hb}^{\lambda_1} - \mu_a^{\lambda_1}\varepsilon_{Hb}^{\lambda_2}}{\mu_a^{\lambda_1}\Delta\varepsilon_{Hb}^{\lambda_2} - \mu_a^{\lambda_2}\Delta\varepsilon_{Hb}^{\lambda_1}} \tag{1}$$

$$HbT = [HbO]+[Hb] = \frac{\mu_a^{\lambda_1}\Delta\varepsilon_{Hb}^{\lambda_2} - \mu_a^{\lambda_2}\Delta\varepsilon_{Hb}^{\lambda_1}}{\varepsilon_{Hb}^{\lambda_1}\varepsilon_{HbO}^{\lambda_2} - \varepsilon_{Hb}^{\lambda_2}\varepsilon_{HbO}^{\lambda_1}} \tag{2}$$

where, μ_a is the absorption coefficient in units of cm^{-1}; ε_{HbO} and ε_{Hb} are the known molar extinction coefficients (in units of cm^{-1} M^{-1}) of HbO and Hb, respectively; $\Delta\varepsilon_{Hb} = \varepsilon_{HbO} - \varepsilon_{Hb}$; and [HbO] and [Hb] are the concentrations (in units of M) of the two forms of hemoglobin, respectively. The optical absorption coefficients were estimated by the PA signal amplitude [46,47]. The latter was estimated by calculating the envelope of the time-domain PA signal within the tumor region of interest. Using a histogram-based quantification approach developed by our group [20,22], the sO_2 and HbT values of each 2D slice within the tumor was calculated from the mode of the sO_2 and HbT histograms, respectively. At every imaging timepoint, the average mode was computed throughout the entire tumor volume for every mouse and then averaged across all animals belonging to the same treatment group to examine inter-treatment variation in tumor oxygen saturation and total hemoglobin level. Additionally, the distribution of the sO_2 and HbT across the tumor volume was also examined by plotting each sO_2 or HbT mode value from 2D images as a single datapoint across multiple treatments/timepoints. Lastly, the differences relative to the pre-treatment timepoint for each mouse was calculated and the percent change from the control mice were computed.

2.5.3. Vessel size and structure biomarkers

The time/spatial domain PA radiofrequency (RF) signals acquired at both wavelengths of illumination $p(x,y,z,\lambda)$ were used to compute the normalized PA power spectrum as a function of acoustic frequency f [22, 48]. The wavelength-dependent, normalized power spectrum at every z^{th} 2D scan of the tumor $PS_{norm}(f,z,\lambda)$ was calculated by:

$$PS_{norm}(f,z,\lambda) = \frac{1}{S}\sum_{i=1}^{S}\mathbf{log}_{10}\left[\frac{PS(f,z_i,\lambda)_{\text{tumor}}}{PS(f,z_i,\lambda)\text{ref}}\right]^2 \tag{3}$$

where, $PS(f,z,\lambda)_{\text{tumor}}$ and $PS(f,z_i,\lambda)_{ref}$ are the power spectra for the tumor and reference phantom, respectively. They were computed by taking the Fast Fourier Transform of all the RF lines comprising each 2D scan within the tumor and the reference phantom. The latter was a gelatin-based construction of black carbon spheres (diameter 1−12 μm) [27] which was imaged at the end of each timepoint using the same imaging settings as the tumors to remove the system dependencies. The normalized power spectra were fitted to a straight line as shown in Fig. 2 and the PA spectral slope (SS) was extracted from:

$$PS_{fit}(f) = SS \times f + Y_{int} \tag{4}$$

where, $PS_{fit}(f)$ is the linear fit obtained from performing linear regression on the $PS_{norm}(f,z,\lambda)$ in the 10−30 MHz -6 dB range of the linear

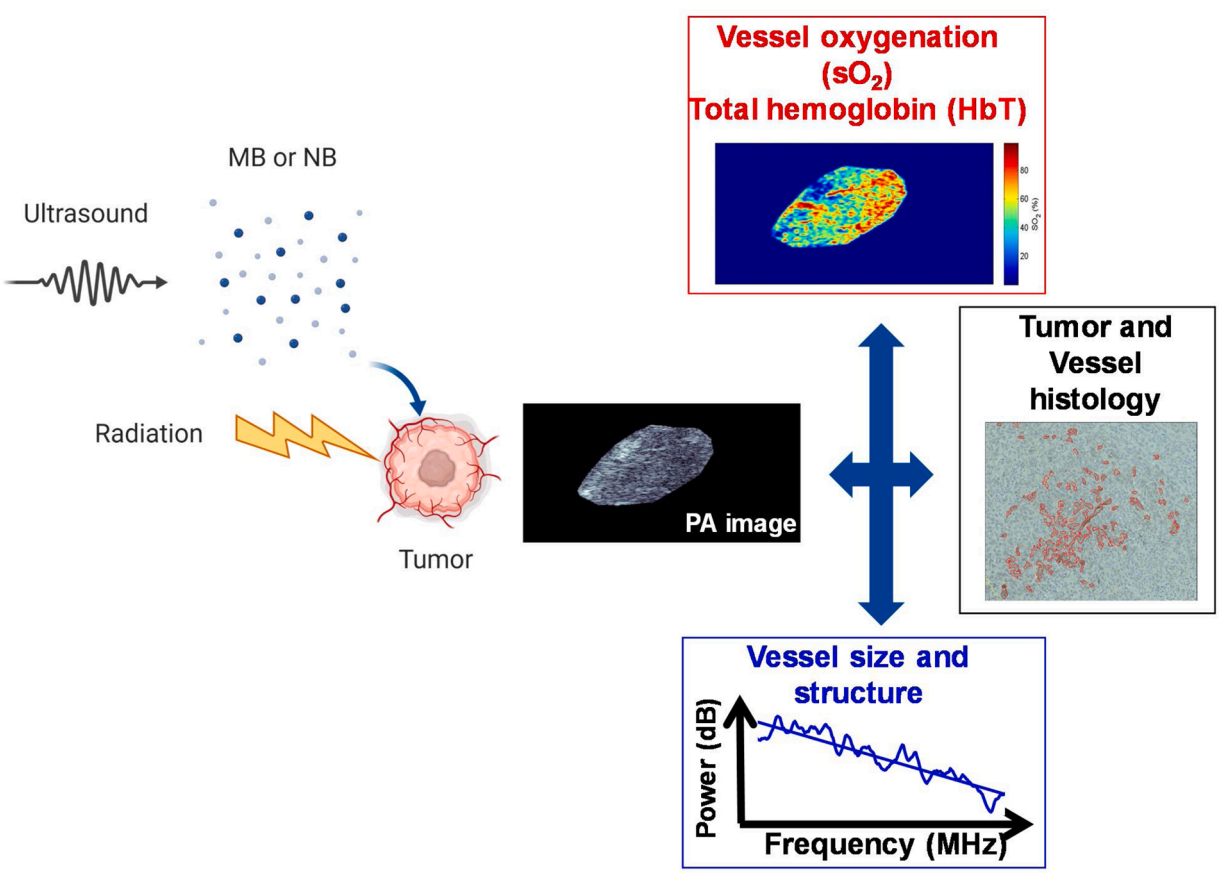

Fig. 2. PA imaging biomarkers of treatment response.
The effects of the combination of ultrasound-simulated MB or NB treatments with radiation can be probed using PA imaging biomarkers (functional and structural) and can be correlated with histological metrics of tumor cells and blood vessels. Treatment and tumor illustrations were created with Biorender.com. Abbreviations: MB = microbubble; NB = nanobubble; sO2 = oxygen saturation; HbT = total hemoglobin.

array probe and Y_{int} is the y-intercept of the fit measured in dB. As was done with the sO_2 and HbT parameters, the average SS value was computed for every 2D scan within the tumor in addition to the percent change from the pre-treatment values and untreated control group. This was done for both wavelengths of illumination 750 and 850 nm to examine the oxygen-dependent trends in SS.

2.6. Histological analyses and correlations with PA imaging

All animals were sacrificed after the 24 h post-treatment imaging timepoint. The excised tumors were fixed in 10 % paraformaldehyde (volume/volume in PBS) overnight and were subsequently embedded in paraffin. Representative sections were taken from the approximate center of each tumor and stained with standard hematoxylin and eosin (H&E). The vasculature of tumors was stained through endothelial cluster of differentiation 31 (CD31) staining (Fig. 3A–C). The degree of apoptotic cell death was assessed by deoxynucleotidyltransferase-mediated-dUNP-biotin nick end labeling (TUNEL) staining (Fig. 3D and E). CD31 is a widely used marker of tumor vascularity that can be used to assess both the vessel density as well as the blood vessel size distribution [49,50]. Similarly, TUNEL is commonly used to quantify cell death within tumors exposed to various cancer treatments [51–53]. Along with H&E, these histological markers have been used successfully used to study the morphology of the tumor vasculature and cancer cells in studies involving PA imaging [54–56]. The H&E, TUNEL and CD31 sections were sequentially acquired within 10 μm of each other.

The slides were digitized using the ZEISS Axio Scan.Z1 (Carl Zeiss Canada, Ltd., Toronto, Canada) brightfield illumination microscope (20x/0.8 Plan-Apochromat objective) attached to a Hitachi 3-chip color camera (Hitachi Kokusai Electric Camera, Ltd., Woodbury, NY, USA). All quantification analysis was performed using the HALO® image analysis platform (Indica Labs, Albuquerque, NM, USA). The tumor areas were manually segmented for each stain while excluding histological folding artifacts and non-tumor regions. Using the area quantification module, the CD31 (Fig. 3B, tumor vascularity) and TUNEL (Fig. 3D, degree of cell death) positive areas were calculated by separating the stain signal from the background signal. This was accomplished by training the HALO® software on the representative CD31, TUNEL or background intensity levels and automatically generating pseudo colored markups for all slides. In order to quantify the size of each CD31 positive 'object' (defined either as a cluster of endothelial cells or a vessel with the lumen intact, refer to Fig. S2), the perimeter of all objects was automatically traced, and a histogram distribution was generated (Fig. 3C). The mode of the histogram was used to compute the average vessel perimeter. The ratio of the area under the curve to the tumor area was used to compute the vascular density of each tumor in units of number of vessels/μm^2.

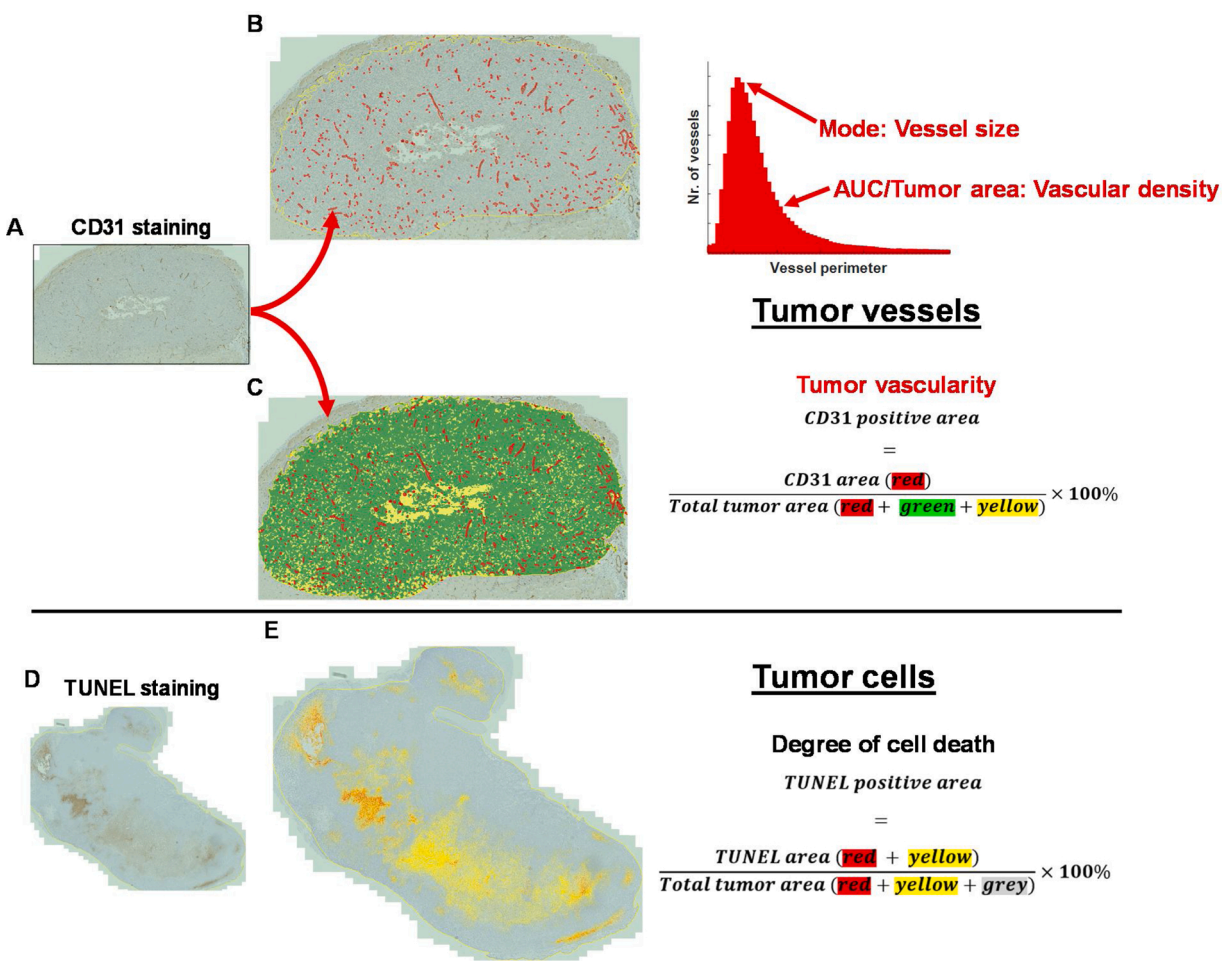

Fig. 3. Histological metrics of tumor vessels and cells.
(**A**) CD31 staining of tumor blood vessels can be used to estimate both the (**B**) vascularity of tumors by measuring the CD31 positive area and (**C**) the vascular density and vessels size by computing the total number and size of each vessel, respectively. The red pseudo color denotes the vessels and green and yellow denote the background and cell free areas, respectively. The cell-free areas are assessed by the presence of the hematoxylin nuclear counterstain. (**D**) TUNEL staining can be quantified by measuring the (**E**) TUNEL positive area in the tumor in order to estimate the extent of cell death. Red and yellow pseudo colors represent different intensities of TUNEL staining. Abbreviations: CD31 = cluster of differentiation 31; AUC = area under curve; TUNEL = Terminal deoxynucleotidyltransferase-mediated-dUNP-biotin nick end labeling.

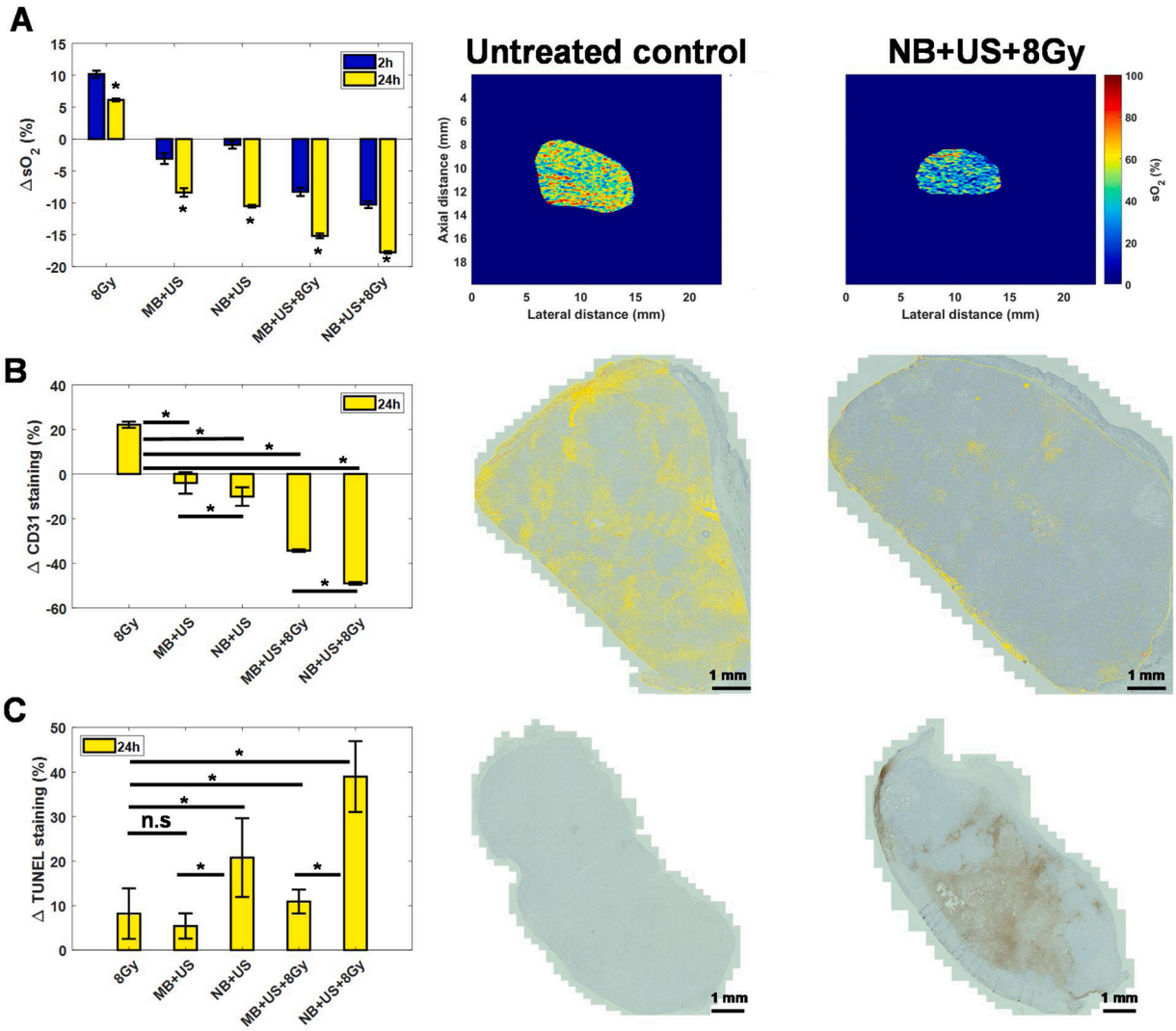

Fig. 4. PA imaging and histological biomarkers of treatment response.
Change in (**A**) PA estimations in tumor sO2, (**B**) CD31 positive area and (**C**) TUNEL positive area relative to the untreated control as a function of treatment and imaging timepoint (sO2 only). The error bars denote the standard error of the mean change for all animals belonging in that treatment group. Statistical significance is doted by * ($p < 0.05$) and n.s. denotes not significant. The sO2 comparisons denote statistical significance between the 2 h and 24 h imaging timepoints. For every biomarker, representative sO2 maps, CD31 and TUNEL histological images are shown for the untreated control and the NB + US+8 Gy treatment. Axial and lateral distances in the sO2 maps are in relation to the imaging transducer.

For each treatment group, the percentage of tumor vascularity, vascular density, average vessel size and tumor cell death were computed at 24 h post-treatment as shown in Fig. 3. These histological metrics were normalized by computing the percentage change relative to the untreated control group. The PA imaging biomarkers were correlated against the histological metrics of treatment response in order to assess the relation between the changes in the imaging biomarkers and the biophysical changes that tumors undergo post-treatment. Correlation plots were also generated between relevant histological metrics (vessel perimeter *vs*. vascular density) and imaging biomarkers (HbT *vs*. sO_2) for every treatment group.

2.7. Statistical analysis

A two-way analysis of variance (ANOVA) test was utilized to determine if the changes in sO_2, CD31 and TUNEL among treatment groups were statistically significant and whether the MB/NB treatments had an effect on the radiation treatment. A variable with a p value of 0.05 was considered statistically significant and post hoc comparisons using Tukey's least significant differences identified 95 % confidence intervals to determine the pairs which were significantly different [57]. All statistical analysis was performed using Matlab 2018b (The MathWorks, Inc., Natick, MA).

3. Results and discussion

3.1. Quantification of micro/nanobubble treatment response

Fig. 4 summarizes the PA-based and histology-based biomarkers post-treatment. The sO_2 at 2- and 24 -hs post-treatment was compared against the untreated control mice (Fig. 4A). All changes relative to the control mice are statistically significant at both timepoints ($p < 0.05$). A single fraction of 8 Gy increases the tumor oxygen saturation by as much as 10 % at 2 h post-treatment, with a subsequent drop in sO_2 at the 24-h timepoint that is still above pre-treatment levels ($p < 0.05$). The oxygen consumption is driven by the metabolic demands of tumor cells with blood flow regulating the oxygen supply [58]. Radiation-induced vascular changes will affect the tumor sO_2 [21] and disrupt endothelial cells [59]. The increase in CD31 staining observed for the 8 Gy group (Fig. 4B) is consistent with an sO_2 increase (Fig. 4A) and is supported by other studies of tumor neovascularization observed post-radiation treatments [60–62]. The acute inflammatory response which is triggered immediately post radiation-induced cellular damage (Fig. 4C) may increase the blood flow to the tumor, increasing the oxyhemoglobin concentration within the tumor, thereby increasing the sO_2.

Czarnota and colleagues have demonstrated that MB + US treatments can be used as radiation-enhancing antivascular agents [39–41]. Endothelial cells lining the tumor blood vessels undergo apoptosis through the release of ceramide in response to radiation exposure [41]. In addition, the ultrasonic-mediated, inertial cavitation of MBs induces vascular damage to the tumors. These vascular effects can be measured through PA sO_2 estimates as shown in Fig. 5A and the CD31 staining in Fig. 5B. The decrease in CD31 staining is most likely related to the reduced vessel integrity, and thus blood flow to the tumor [40], leading to a decrease in the supply of oxygenated blood and thus, oxygenated hemoglobin. As the PA imaging biomarkers are sensitive to the oxygenation of the red blood cells, it can measure this treatment-induced vascular effect.

NBs have shown promise as contrast agents [32]. This study presents the first time nanobubbles are used as vascular disrupting agents. As shown in Fig. 4A and B, the NB + US treatments induce a vascular effect that is stronger than the MB + US treatments (10.3 % in tumor sO_2 and 10 % drop in CD31 compared to 7.7 % and 4 % for MBs, respectively). This suggests that the NB + US exposure impacts the tumor vascularity in a manner similar to MBs, possibly inducing damage to blood vessels due to inertial cavitation in the vicinity of endothelial cells.

The combination of radiation with the MB and NB treatments amplifies the decrease in tumor oxygenation (as assessed by sO_2) and vascularity. The largest decrease in sO_2 (18 %) was observed for the NB + US+8 Gy treatment at 24 h post-treatment (Fig. 4A) while the

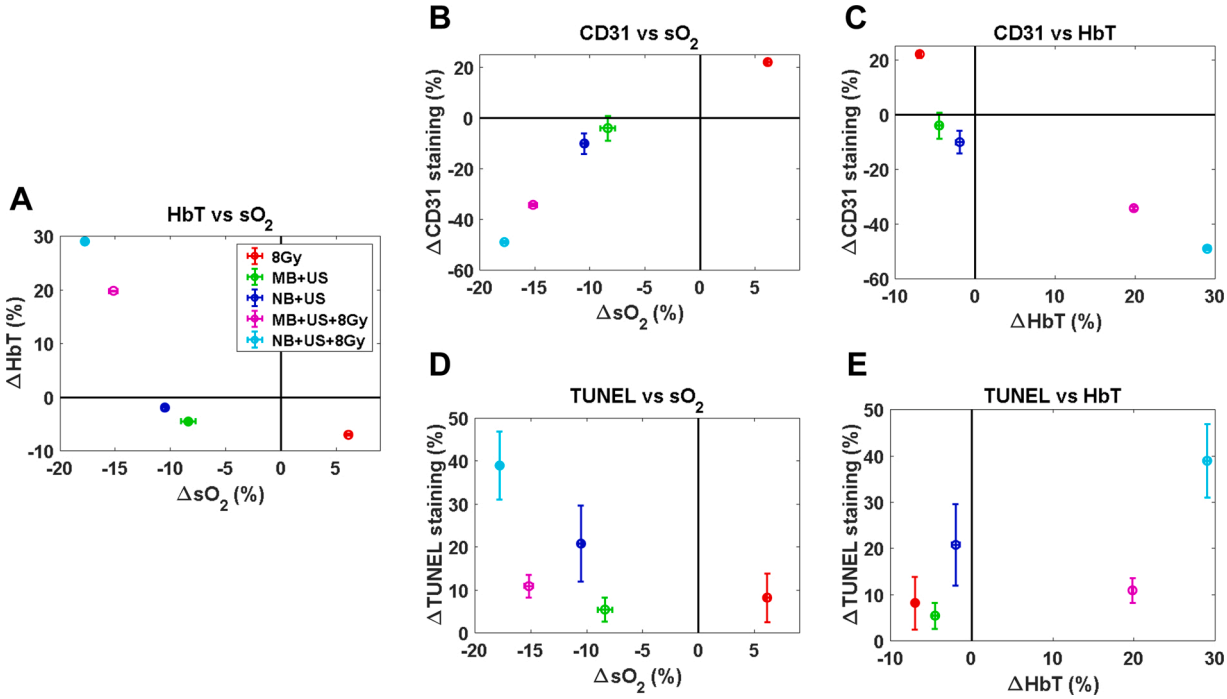

Fig. 5. Impact of treatments on oxygenation metrics.
Correlations between the changes in (**A**) HbT and sO2, (**B**) CD31 and sO2, (**C**) CD31 and HbT, (**D**) TUNEL and sO2, and (**E**) TUNEL and sO2. Each parameter change is measured at 24 h post-treatment and is calculated relative to the untreated control, for all treatment groups. Error bars denote the standard error of the mean change for all animals belonging in that treatment group.

tumor vascularity assessed by CD31 staining decreased by nearly 50 % at the same timepoint (Fig. 4B). The tumor sO_2 decreased as early as 2 h post-exposure for all bubble treatments. The drop in sO_2 for the NB + US+8 Gy treatment was approximately 10 % greater compared to the NB + US treatment at both 2- and 24-hs post-treatment. These changes were also mirrored by changes in the CD31 staining (Fig. 4B), all of which are significantly lower than the single 8 Gy fraction of radiation. These findings support the hypothesis that ultrasonically simulated bubbles impact the vasculature of tumors [39].

Histological analysis of tumors post-treatment offers insights into the mechanism of action for each treatment. Fig. 4C shows the degree of cell death as a result of radiation, MB and NB treatments. As observed by the representative images of TUNEL staining for untreated control and NB + US+8 Gy treatments, there is a notable increase in brown staining. Quantification of this apoptotic stain reveals more than 2-fold higher degree of cell death for the NB + US group compared to the MB + US counterpart ($p < 0.05$). This observation suggests that the NBs, for these ultrasound exposure parameters and bubble concentrations, are more effective at damaging the tumor cells than MBs, perhaps due to their ability to extravasate into the tumor interstitium [42]. When combined with radiation, the NB + US+8 Gy treatment exhibited, on average, 40 % more cell death compared to the untreated control 24 h post-treatment. Apart from the MB + US treatment, all other treatments had a significantly higher degree of cellular death compared to the single fraction of radiation ($p < 0.05$). The vascular disruption from the cavitation of MBs and NBs leads to a drop in the tumor sO_2 as measured by PA imaging. When accompanied by the radiation damage, this leads to an increase in tumor cell death.

3.2. Changes in functional biomarkers during treatment

The tumor vessel oxygenation has been previously showed as a reliable biomarker of cancer treatment response [18,20,21]. In order to further explore the biophysical mechanism of the MB and NB treatments, Fig. 5 shows a direct comparison between PA biomarkers of tumor oxygenation (sO_2 and HbT) and histologically measured biomarkers of tumor blood vessels (CD31) and cell death (TUNEL). Simultaneous sO_2 and HbT measurements in the same imaging plane reveal an inverse relationship between the two (Fig. 5A). As the oxygenation of tumors decreases, there a significant increase in the concentration of total hemoglobin present in the tumor. A nearly 20 % decrease in tumor sO_2 (NB + US+8 Gy) is accompanied by nearly 30 % in HbT. Total hemoglobin has been shown to correlate with the overall blood volume in biological tissue [9,45,63,64]. In the case of MB- and NB-enhanced radiation treatments, the disruption of the vasculature might lead to the hemorrhaging of red blood cells in the tumor interstitium. The decrease in CD31 staining when the tumor sO_2 decreases (Fig. 5B) and the HbT increases (Fig. 5C) also supports this hypothesis. These results also suggest that there is a threshold of CD31 staining (~20 %), beyond which the vascular damage induces an increase in HbT, potentially due to hemorrhaging. This may be probed further through dose-dependent studies in both MB/NB concentration and radiation dose [40].

We then examined the relationship between tumor cell death (as assessed by TUNEL staining), the tumor sO_2 (Fig. 5D) and HbT (Fig. 5E). The tumors which exhibited the largest degree of cellular death were also the ones with the largest drop in oxygenation and the largest increase in total HbT. Much like the changes in tumor vascularity (as assessed by CD31 staining), the functional PA-measured biomarkers are correlated with the degree of cell death. NB cavitation can affect the integrity of the endothelial cells, modifying the tumor vascularity. Their extravasation into the tumor interstitium allows them to be in close proximity to the tumor cells. Ultrasonic cavitation of gas filled bubbles has been shown to induce cellular death through sonoporation and related mechanisms [43], consistent with the hypothesis that NBs can act as anticancer agents. Fig. 6 supports these findings by plotting the tumor size after NB-derived treatments. The NB + US+8 Gy treatment yielded the largest growth delay, observable as early as 12 days post-treatment where a 26 % decrease in tumor volume was recorded. The ultrasound-activated nanobubble treatments and the radiation alone treatment also delay the growth of the tumor in comparison to the untreated control. By day 30 post-treatment, the NB + US+8 Gy had reduced the tumor volume by more than 70 %. These observations are consistent with previously published results describing the growth delay effects of US + MB+8 Gy treatments [40]. In order to examine the efficacy of NB-mediated radiation therapy in comparison to the MB equivalent treatment, rigorous comparisons must be conducted and are planned for future work. For instance, one must equalize the gas volume encapsulated within MBs and NBs in order to directly compare them [65,66].

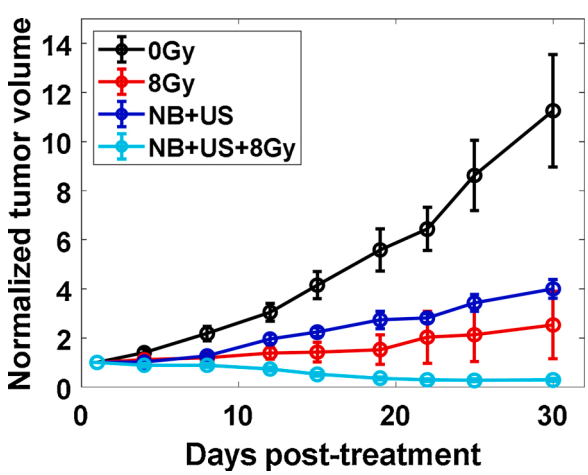

Fig. 6. Tumor growth delay data for single nanobubble and radiation treatments.
The tumor volumes were normalized to the size of the tumor on day 1 post-treatment, for each respective group. The error bars denote the standard error of the mean.

3.3. Changes in structural biomarkers during treatments

Our group has demonstrated that PA imaging biomarkers can be used to study tumor blood vessels [22,28]. MB and NB treatments appear to impact the structural integrity of tumor vasculature [41]. Fig. 7 summarizes the histologically measured structural vessel parameters (perimeter and density) as a function of the PA-measured biomarkers (sO_2, HbT and SS). The vascular density after the MB and NB treatments decreases, while the vascular density after the 8 Gy radiation dose increases (Fig. 7A). However, the perimeter of vessels (assessed by CD31 staining, Fig. S2) is higher for MB treatments compared to NBs. The addition of radiation decreases vascular density for both the MB + US+8 Gy and NB + US+8 Gy treatments when compared to MB + US and NB + US, respectively.

The histologically measured changes in the tumor vascular network can be also probed through PA biomarkers. Specifically, the vascular density is correlated with the tumor sO_2 (Fig. 7B) and HbT (Fig. 7C). The nearly 20 % drop in tumor sO_2 for the NB + XRT+8 Gy group is likely due to the destruction of blood vessels. This is supported by an 80 % drop in the vascular density (Fig. 7B). Moreover, as blood vessels lose their integrity, hemorrhaging of the red blood cells creates interstitial blood pooling [22,54]. This in turn causes the total hemoglobin in the tumor to increase by nearly 30 % (Fig. 7C) as blood flowing into the tumor leaks out and accumulates outside of damaged vessels.

Our group and others have demonstrated experimentally and through simulations that the PA spectral slope is sensitive to the size of

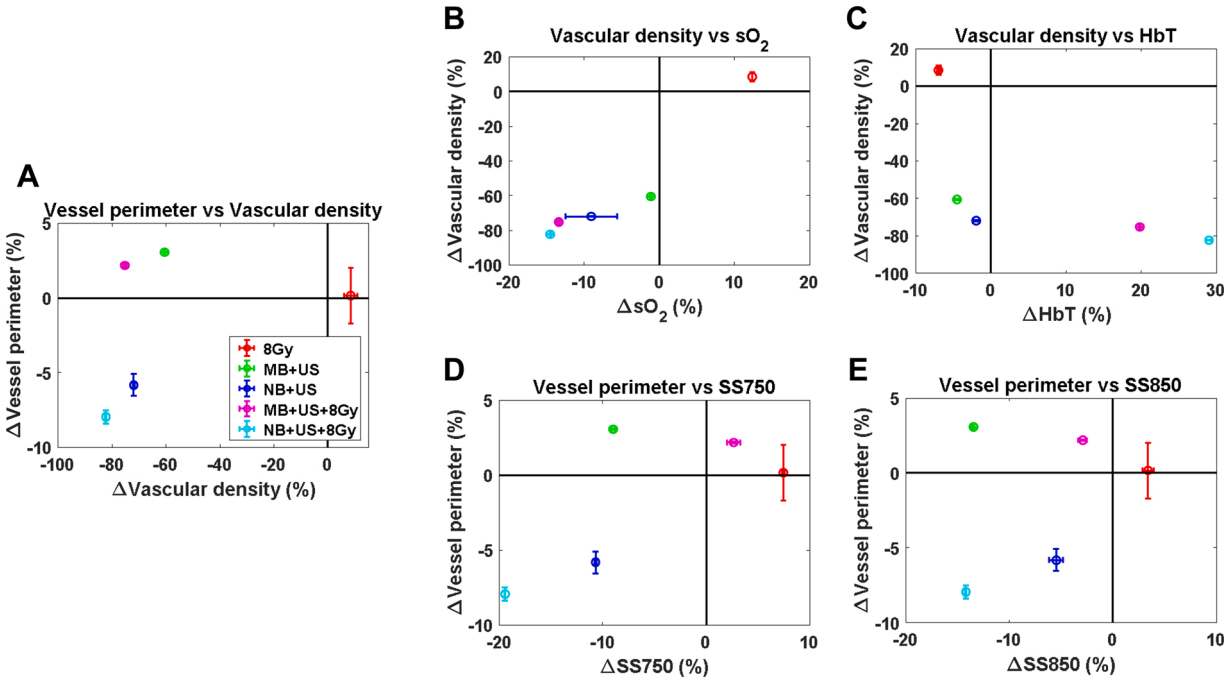

Fig. 7. Impact of treatments on tumor vascularity.
Correlations between the changes in (**A**) Vessel perimeter and Vascular density, (**B**) Vascular density and sO2, (**C**) Vascular density and HbT, (**D**) Vascular density and SS at 750 nm and (**E**) Vascular density and SS at 850 nm. Each parameter change is measured at 24 h post-treatment and is calculated relative to the untreated control, for all treatment groups. Error bars denote the standard error of the mean change for all animals belonging in that treatment group.

the source of PA signals [28,48,67]. Here we examine how the SS may be used to characterize the changes in vessel size post radiation, MB and NB treatments. Fig. 7D and E summarizes the changes in SS and vessel perimeter at 750 nm and 850 nm illuminations, respectively. Much like the histologic metrics shown in Fig. 7A, the PA SS can also be used to differentiate between the effects MB and NB-based treatments. Fig. S3 plots the absolute values of the pre-and post-treatment SS values reflecting the changes observed in Fig. 7.

The SS decreases at both illumination wavelengths for both the MB + US and NB + US groups. A decrease in the SS has been previously linked to an increase effective absorber size as was shown through simulations and experiments by our group [28]. In the context of vascular targeted treatments, we have shown that when tumors hemorrhage, the effective absorber size (*i.e.* pools of red blood cells) increases [22,68]. The SS and vessel perimeter changed post-treatment further provide evidence that both the MB and NB treatments induce changes in the tumor vasculature. Using CD31 staining post-treatment, one can assess the size of the remaining vessels (*i.e.* endothelial cells which we hypothesize survived the MB/NB disruption). Fig. 7D and E shows the changes in SS and vessel perimeter. The perimeter of the remaining vessels after the MB treatments is larger than the perimeter before treatment, whereas perimeter of the remaining vessels after the NB treatments is smaller than before the treatment. For both treatments, the vascular density is significantly reduced. Moreover, the SS drop for the tumors exposed to MB treatments is smaller than for the NB treatments. The difference in the change in SS between the treatments suggests that the MB and NB treatments affect different levels of the tumor vasculature, most likely due to the different size of the MBs (3 μm) compared to NBs (200 nm).

Moreover, differences in the changes in the SS arise between the 750 and 850 nm illuminations for both NB and MB treatments. At 750 nm, the decrease in spectral slope for the NB treatments is greater than at 850 nm. For 750 nm, the wavelength for which deoxygenated hemoglobin has a higher molar extinction coefficient [69], the decrease in spectral slope is greater. This might be an indication of larger pools of deoxygenated blood due to hemorrhaging. The decrease in both vessel perimeter and CD31 staining for NB treatments would support the hemorrhaging hypothesis, especially when considering the increase in HbT with the treatments with radiation.

Conversely, for the MB treatments, at 750 nm the decrease in spectral slope is less than at 850 nm. At 850 nm, oxygenated hemoglobin has a higher molar extinction coefficient and contributes more to the PA signal, and therefore red blood cells outside the hemorrhagic pool would contribute more to the signal. The increase in the vessel perimeter and decrease in CD31 staining for MB treatments would indicate for the MB treatments there is less hemorrhage compared to the NB treatments. A wavelength dependence in the SS has been observed when monitoring PA sources of different absorption properties such as fat deposits in the liver [48] or benign tumors in ovarian tissues [70]. In this work, the difference between the SS at both wavelengths can be attributed to the oxygen dependence of hemoglobin, the most abundant absorber inside red blood cells [69].

4. Conclusions and prospects on clinical translation

The goal of this work is to develop acoustic resolution photoacoustic imaging biomarkers of cancer treatment response for microbubble and nanobubble mediated radiosensitization. We designed experiments to gain insight into the structural and biochemical tissue modifications that drive the changes in photoacoustic imaging. This was accomplished by correlating the imaging biomarker treatment-induced changes to histological metrics of cancer treatment response. PA imaging biomarkers were used to differentiate tumor response between the microbubble and nanobubble radiosensitization treatments. Imaging biomarkers of tumor oxygenation and vascular structure are linked to the structural and biochemical changes that the blood vessels undergo upon radiation-treatment after bubble stimulation. The nanobubble-radiation combined treatment results in twice as much cellular death compared to the

nanobubble treatment alone. Nanobubble treatments also show enhanced cell kill compared to the microbubble treatments for the exposure parameters and bubble concentrations used in these experiments.

The results offer new insights into the functional and structural changes of tissue that form the basis of photoacoustic imaging biomarkers for early cancer treatment monitoring. Even when acoustic resolution PA imaging is used, which cannot be used to resolve the microvasculature, imaging biomarkers of treatment response can be developed to assist in clinical decision making. A limitation of all PA imaging remains the limited imaging penetration depth, which makes the imaging of deep-seated tumors challenging. Advances in light delivery technologies have enabled PA imaging to successfully image the entire breast [10], the intestines [71,72], prostate [73] and even human kidneys in transplantation settings [74]. Therefore, it should be, in principle, possible to track the progression of cancer treatments for deeper-seated tumors.

For both therapy and imaging, consideration must be given to the nanobubble circulation time. Our group has demonstrated that the circulation time of nanobubbles in pre-clinical tumor models is approximately six-times longer than that of conventional microbubbles, circulating for at least 30 min after injection [32,42,75]. Prior to clinical translation of this treatment approach, efficacy studies must be conducted to determine the optimal concentration and ultrasonic treatment parameters.

Declaration of Competing Interest

The authors declare that there are no conflicts of interest.

CRediT authorship contribution statement

Eno Hysi: Conceptualization, Methodology, Software, Validation, Formal analysis, Investigation, Data curation, Writing - original draft, Writing - review & editing, Visualization. **Muhannad N. Fadhel:** Methodology, Software, Validation, Writing - review & editing. **Yanjie Wang:** Methodology, Validation, Writing - review & editing. **Joseph A. Sebastian:** Methodology, Software, Validation, Writing - review & editing. **Anoja Giles:** Methodology, Data curation, Resources. **Gregory J. Czarnota:** Conceptualization, Resources, Writing - review & editing, Supervision, Project administration, Funding acquisition. **Agata A. Exner:** Conceptualization, Resources, Writing - review & editing, Funding acquisition. **Michael C. Kolios:** Conceptualization, Resources, Writing - review & editing, Supervision, Project administration, Funding acquisition.

Acknowledgments

This research was undertaken, in part, through grants provided by the Terry Fox Foundation through a Program Project Grant funded through the Hecht Foundation (GJC and MCK), National Institutes of Health (AAE and MCK) and the Natural Sciences and Engineering Research Council of Canada (MCK). EH held a Vanier Canada Graduate Scholarship during the conduct of this research. MF was supported through an NSERC Alexander Graham Bell Graduate Scholarship. The authors would like to acknowledge the assistance of Dr. Azza Al-Mahrouki, Dr. Lauren Wirtzfeld and Nikki Law. The Keenan Research Centre Core Facilities at St. Michael's Hospital and Dr. Caterina Di Ciano-Oliveira are acknowledged for assistance with histological analysis. The technical support provided by the Toronto office of Fujifilm-VisualSonics is also gratefully recognized.

Appendix A. Supplementary data

Supplementary material related to this article can be found, in the online version, at doi:https://doi.org/10.1016/j.pacs.2020.100201.

References

[1] M.B. Amin, F.L. Greene, S.B. Edge, et al., The Eighth Edition AJCC Cancer staging Manual: continuing to build a bridge from a population-based to a more 'personalized' approach to cancer staging, CA Cancer J. Clin. 67 (2017) 93–99.
[2] D. Cross, J.K. Burmester, Gene therapy for cancer treatment: past, present and future, Clin. Med. Res. 4 (2006) 218–227.
[3] J.J. Smith, A.G. Sorensen, J.H. Thrall, Biomarkers in imaging: realizing radiology's future, Radiology 227 (2003) 633–638.
[4] Precision Medicine Initiative [Internet]. National Institutes of Health (NIH). 2015 [cited 27 April 2016]. Available at: https://www.nih.gov/precision-medicine-initiative-cohort-program.
[5] E.I. Dumbrava, F. Meric-Bernstam, Personalized cancer therapy—leveraging a knowledge base for clinical decision-making, Cold Spring Harb. Mol. Case Stud. (2018) [Internet] [cited 28 December 2019] 4. Available at: https://www.ncbi.nlm.nih.gov/pmc/articles/PMC5880252/.
[6] M. Verma, Personalized medicine and cancer, J. Pers. Med. 2 (2012) 1–14.
[7] C.L. Vogel, M.A. Cobleigh, D. Tripathy, et al., Efficacy and safety of trastuzumab as a single agent in first-line treatment of HER2-overexpressing metastatic breast cancer, J. Clin. Oncol. Off. J. Am. Soc. Clin. Oncol. 20 (2002) 719–726.
[8] R.K. Jain, Normalizing tumor microenvironment to treat cancer: bench to bedside to biomarkers, J. Clin. Oncol. 31 (2013) 2205–2218.
[9] T. Vu, D. Razansky, J. Yao, Listening to tissues with new light: recent technological advances in photoacoustic imaging, J. Opt. 21 (2019), 103001.
[10] L. Lin, P. Hu, J. Shi, et al., Single-breath-hold photoacoustic computed tomography of the breast, Nat. Commun. 9 (2018) 2352.
[11] A. Taruttis, S. Morscher, N.C. Burton, D. Razansky, V. Ntziachristos, Fast multispectral optoacoustic tomography (MSOT) for dynamic imaging of pharmacokinetics and biodistribution in multiple organs. Prow TW, Ed, PLoS One 7 (2012), e30491.
[12] M. Nasiriavanaki, J. Xia, H. Wan, A.Q. Bauer, J.P. Culver, L.V. Wang, High-resolution photoacoustic tomography of resting-state functional connectivity in the mouse brain, Proc. Natl. Acad. Sci. 111 (2014) 21–26.
[13] C. Cai, K.A. Carey, D.A. Nedosekin, et al., In vivo photoacoustic flow cytometry for early malaria diagnosis, Cytom. Part J. Int. Soc. Anal. Cytol. (2016).
[14] M. Heijblom, D. Piras, W. Xia, et al., Visualizing breast cancer using the Twente photoacoustic mammoscope: what do we learn from twelve new patient measurements? Opt. Express 20 (2012) 11582–11597.
[15] M. Heijblom, D. Piras, M. Brinkhuis, et al., Photoacoustic image patterns of breast carcinoma and comparisons with Magnetic Resonance Imaging and vascular stained histopathology, Sci. Rep. 5 (2015) 11778.
[16] E.I. Neuschler, R. Butler, C.A. Young, et al., A pivotal study of optoacoustic imaging to diagnose benign and malignant breast masses: a new evaluation tool for radiologists, Radiology. (2017), 172228.
[17] S. Manohar, M. Dantuma, Current and future trends in photoacoustic breast imaging, Photoacoustics 16 (2019), 100134.
[18] S. Mallidi, K. Watanabe, D. Timerman, D. Schoenfeld, T. Hasan, Prediction of tumor recurrence and therapy monitoring using ultrasound-guided photoacoustic imaging, Theranostics 5 (2015) 289–301.
[19] P. Shao, D.W. Chapman, R.B. Moore, R.J. Zemp, Monitoring photodynamic therapy with photoacoustic microscopy, J. Biomed. Opt. 20 (2015), 106012.
[20] J.P. May, E. Hysi, L.A. Wirtzfeld, E. Undzys, S.-D. Li, M.C. Kolios, Photoacoustic imaging of cancer treatment response: early detection of therapeutic effect from thermosensitive liposomes, PLoS One 11 (2016), e0165345.
[21] L.J. Rich, M. Seshadri, Photoacoustic monitoring of tumor and normal tissue response to radiation, Sci. Rep. 6 (2016) 21237.
[22] E. Hysi, L.A. Wirtzfeld, J.P. May, E. Undzys, S.-D. Li, M.C. Kolios, Photoacoustic signal characterization of cancer treatment response: correlation with changes in tumor oxygenation, Photoacoustics 5 (2017) 25–35.
[23] F.L. Lizzi, M. Ostromogilsky, E.J. Feleppa, M.C. Rorke, M.M. Yaremko, Relationship of ultrasonic spectral parameters to features of tissue microstructure, IEEE Trans. Ultrason. Ferroelectr. Freq. Control 34 (1987) 319–329.
[24] J. Mamou, M.L. Oelze (Eds.), Quantitative Ultrasound in Soft Tissues, Springer Netherlands, Dordrecht, 2013 [Internet] [cited 3 December 2015]. Available at: http://link.springer.com/10.1007/978-94-007-6952-6.
[25] G.J. Diebold, M.I. Khan, S.M. Park, Photoacoustic 'signatures' of particulate matter: optical production of acoustic monopole radiation, Science 250 (1990) 101–104.
[26] E.M. Strohm, I. Gorelikov, N. Matsuura, M.C. Kolios, Modeling photoacoustic spectral features of micron-sized particles, Phys. Med. Biol. 59 (2014) 5795–5810.
[27] E. Hysi, D. Dopsa, M.C. Kolios, Photoacoustic tissue characterization using envelope statistics and ultrasonic spectral parameters, Proc SPIE (2014), https://doi.org/10.1117/12.2038624 [Internet] [cited 30 June 2016]. Available at:.
[28] E. Hysi, M.N. Fadhel, M.J. Moore, J. Zalev, E.M. Strohm, M.C. Kolios, Insights into photoacoustic speckle and applications in tumor characterization, Photoacoustics 14 (2019) 37–48.
[29] C. Bing, Y. Hong, C. Hernandez, et al., Characterization of different bubble formulations for blood-brain barrier opening using a focused ultrasound system with acoustic feedback control, Sci. Rep. 8 (2018) 1–12.
[30] P. Nittayacharn, H.-X. Yuan, C. Hernandez, P. Bielecki, H. Zhou, A.A. Exner, Enhancing tumor drug distribution with ultrasound-triggered nanobubbles, J. Pharm. Sci. 108 (2019) 3091–3098.
[31] C. Hernandez, E.C. Abenojar, J. Hadley, et al., Sink or float? Characterization of shell-stabilized bulk nanobubbles using a resonant mass measurement technique, Nanoscale 11 (2019) 851–855.

[32] A. de Leon, R. Perera, C. Hernandez, et al., Contrast enhanced ultrasound imaging by nature-inspired ultrastable echogenic nanobubbles, Nanoscale 11 (2019) 15647–15658.
[33] X. Liang, Y. Xu, C. Gao, Y. Zhou, N. Zhang, Z. Dai, Ultrasound contrast agent microbubbles with ultrahigh loading capacity of camptothecin and floxuridine for enhancing tumor accumulation and combined chemotherapeutic efficacy, NPG Asia Mater. 10 (2018) 761–774.
[34] C. Holland, Ultrasound contrast agents accelerate sonothrombolysis, Ultrasound Med. Biol. 41 (2015) S94.
[35] K. Hynynen, N. McDannold, N. Vykhodtseva, F.A. Jolesz, Noninvasive MR imaging-guided focal opening of the blood-brain barrier in rabbits, Radiology 220 (2001) 640–646.
[36] A.J. Sojahrood, L. Nieves, C. Hernandez, A. Exner, M.C. Kolios, Theoretical and experimental investigation of the nonlinear dynamics of nanobubbles excited at clinically relevant ultrasound frequencies and pressures: the role of lipid shell buckling, 2017 IEEE International Ultrasonics Symposium (IUS) (2017).
[37] R.K. Jain, Delivery of molecular and cellular medicine to solid tumors, Adv. Drug Deliv. Rev. 64 (2012) 353–365.
[38] Y. Gao, C. Hernandez, H.-X. Yuan, et al., Ultrasound molecular imaging of ovarian cancer with CA-125 targeted nanobubble contrast agents, Nanomed. Nanotechnol. Biol. Med. 13 (2017) 2159–2168.
[39] J. Lee, R. Karshafian, N. Papanicolau, A. Giles, M.C. Kolios, G.J. Czarnota, Quantitative ultrasound for the monitoring of novel microbubble and ultrasound radiosensitization, Ultrasound Med. Biol. 38 (2012) 1212–1221.
[40] G.J. Czarnota, R. Karshafian, P.N. Burns, et al., Tumor radiation response enhancement by acoustical stimulation of the vasculature, Proc. Natl. Acad. Sci. U. S. A. 109 (2012) E2033–E2041.
[41] A.A. Al-Mahrouki, S. Iradji, W.T. Tran, G.J. Czarnota, Cellular characterization of ultrasound-stimulated microbubble radiation enhancement in a prostate cancer xenograft model, Dis. Model. Mech. 7 (2014) 363–372.
[42] H. Wu, E.C. Abenojar, R. Perera, A.C. De Leon, T. An, A.A. Exner, Time-intensity-curve analysis and tumor extravasation of nanobubble ultrasound contrast agents, Ultrasound Med. Biol. 45 (2019) 2502–2514.
[43] R. Karshafian, P.D. Bevan, R. Williams, S. Samac, P.N. Burns, Sonoporation by ultrasound-activated microbubble contrast agents: effect of acoustic exposure parameters on cell membrane permeability and cell viability, Ultrasound Med. Biol. 35 (2009) 847–860.
[44] A. Needles, A. Heinmiller, J. Sun, et al., Development and initial application of a fully integrated photoacoustic micro-ultrasound system, IEEE Trans. Ultrason. Ferroelectr. Freq. Control 60 (2013) 888–897.
[45] X. Wang, X. Xie, G. Ku, L.V. Wang, G. Stoica, Noninvasive imaging of hemoglobin concentration and oxygenation in the rat brain using high-resolution photoacoustic tomography, J. Biomed. Opt. 11 (2006), 024015.
[46] L. Wang, K. Maslov, W. Xing, A. Garcia-Uribe, L.V. Wang, Video-rate functional photoacoustic microscopy at depths, J. Biomed. Opt. 17 (2012) 1060071–1060075.
[47] B. Cox, J.G. Laufer, S.R. Arridge, P.C. Beard, Quantitative spectroscopic photoacoustic imaging: a review, J. Biomed. Opt. 17 (2012), 061202.
[48] G. Xu, Z.-X. Meng, J.D. Lin, et al., The functional pitch of an organ: quantification of tissue texture with photoacoustic Spectrum analysis, Radiology 271 (2014) 248–254.
[49] A. de la Taille, A.E. Katz, E. Bagiella, et al., Microvessel density as a predictor of PSA recurrence after radical prostatectomy. A comparison of CD34 and CD31, Am. J. Clin. Pathol. 113 (2000) 555–562.
[50] J. Xing, W. He, Y.-W. Ding, Y. Li, Y.-D. Li, Correlation between contrast-enhanced ultrasound and microvessel density via CD31 and CD34 in a rabbit VX2 lung peripheral tumor model, Med. Ultrason. 20 (2018) 37–42.
[51] D.T. Loo, In situ detection of apoptosis by the TUNEL assay: an overview of techniques, in: V.V. Didenko (Ed.), DNA Damage Detection In Situ, Ex Vivo, and In Vivo: Methods and Protocols, Humana Press, Totowa, NJ, 2011 [cited 22 June 2020]: 3–13. (Methods in Molecular Biology). [Internet] Available at: https://doi.org/10.1007/978-1-60327-409-8_1.
[52] J. Lawry, Detection of apoptosis by the TUNEL assay, in: S.P. Langdon (Ed.), Cancer Cell Culture: Methods and Protocols, Humana Press, Totowa, NJ, 2004 [cited 22 June 2020]: 183–190. (Methods in Molecular Medicine™). [Internet] Available at: https://doi.org/10.1385/1-59259-406-9:183.
[53] Y.-G. Yuan, Q.-L. Peng, S. Gurunathan, Silver nanoparticles enhance the apoptotic potential of gemcitabine in human ovarian cancer cells: combination therapy for effective cancer treatment, Int. J. Nanomed. 12 (2017) 6487–6502.
[54] A. Bar-Zion, M. Yin, D. Adam, F.S. Foster, Functional flow patterns and static blood pooling in tumors revealed by combined contrast-enhanced ultrasound and photoacoustic imaging, Cancer Res. 76 (2016) 4320–4331.
[55] J. Li, A. Chekkoury, J. Prakash, et al., Spatial heterogeneity of oxygenation and haemodynamics in breast cancer resolved in vivo by conical multispectral optoacoustic mesoscopy, Light Sci. Appl. 9 (2020) 57.
[56] K. Haedicke, L. Agemy, M. Omar, et al., High-resolution optoacoustic imaging of tissue responses to vascular-targeted therapies, Nat. Biomed. Eng. 4 (2020) 286–297.
[57] G.A.F. Seber, A.J. Lee, Linear Regression Analysis, John Wiley & Sons, 2012.
[58] H.J. Park, R.J. Griffin, S. Hui, S.H. Levitt, C.W. Song, Radiation-induced vascular damage in tumors: implications of vascular damage in ablative hypofractionated radiotherapy (SBRT and SRS), Radiat. Res. 177 (2012) 311–327.
[59] Y. Liu, Y. Liu, C. Sun, et al., Carbon ion radiation inhibits glioma and endothelial cell migration induced by secreted VEGF, PLoS One 9 (2014), e98448.
[60] O.V. Solesvik, E.K. Rofstad, T. Brustad, Vascular changes in a human malignant melanoma xenograft following single-dose irradiation, Radiat. Res. 98 (1984) 115–128.
[61] M.H.M. Janssen, H.J.W.L. Aerts, R.G.J. Kierkels, et al., Tumor perfusion increases during hypofractionated short-course radiotherapy in rectal cancer: sequential perfusion-CT findings, Radiother. Oncol. J. Eur. Soc. Ther. Radiol. Oncol. 94 (2010) 156–160.
[62] A.G. Orlova, A.V. Maslennikova, G.Y. Golubiatnikov, et al., Diffuse optical spectroscopy assessment of rodent tumor model oxygen state after single-dose irradiation, Biomed. Phys. Eng. Express 5 (2019), 035010.
[63] G. Diot, S. Metz, A. Noske, et al., Multispectral optoacoustic tomography (MSOT) of human breast Cancer, Clin. Cancer Res. Off. J. Am. Assoc. Cancer Res. 23 (2017) 6912–6922.
[64] E. Amidi, A. Mostafa, S. Nandy, et al., Classification of human ovarian cancer using functional, spectral, and imaging features obtained from in vivo photoacoustic imaging, Biomed. Opt. Express 10 (2019) 2303–2317.
[65] B. Cheng, C. Bing, Y. Xi, B. Shah, A.A. Exner, R. Chopra, Influence of nanobubble concentration on blood–Brain barrier opening using focused ultrasound under real-time acoustic feedback control, Ultrasound Med. Biol. 45 (2019) 2174–2187.
[66] E.C. Abenojar, I. Bederman, A.C. de Leon, et al., Theoretical and experimental gas volume quantification of micro- and nanobubble ultrasound contrast agents, Pharmaceutics (2020) 12.
[67] G. Yang, E. Amidi, W. Chapman, et al., Co-registered photoacoustic and ultrasound imaging of human colorectal cancer, J. Biomed. Opt. 24 (2019) 1–13.
[68] M.N. Fadhel, E. Hysi, J. Zalev, M.C. Kolios, Photoacoustic simulations of microvascular bleeding: spectral analysis and its application for monitoring vascular-targeted treatments, J. Biomed. Opt. 24 (2019) 1–8.
[69] S. Prahl, Tabulated data from various sources, http://omlc.ogi.edu/spectra.
[70] X. Leng, W. Chapman, B. Rao, et al., Feasibility of co-registered ultrasound and acoustic-resolution photoacoustic imaging of human colorectal cancer, Biomed. Opt. Express 9 (2018) 5159–5172.
[71] F. Knieling, C. Neufert, A. Hartmann, et al., Multispectral optoacoustic tomography for assessment of Crohn's disease activity, N. Engl. J. Med. 376 (2017) 1292–1294.
[72] Y. Zhu, L.A. Johnson, J.M. Rubin, et al., Strain-photoacoustic imaging as a potential tool for characterizing intestinal fibrosis, Gastroenterology 157 (2019) 1196–1198.
[73] S.-R. Kothapalli, G.A. Sonn, J.W. Choe, et al., Simultaneous transrectal ultrasound and photoacoustic human prostate imaging, Sci. Transl. Med. (2019) [Internet] [cited 24 June 2020]; 11. Available at: https://stm.sciencemag.org/content/11/507/eaav2169.
[74] E. Hysi, X. He, M.N. Fadhel, et al., Photoacoustic imaging of kidney fibrosis for assessing pretransplant organ quality, JCI Insight 5 (2020) [Internet] Available at: https://insight.jci.org/articles/view/136995.
[75] R.H. Perera, A. de Leon, X. Wang, et al., Real time ultrasound molecular imaging of prostate cancer with PSMA-targeted nanobubbles, Nanomed. Nanotechnol. Biol. Med. 28 (2020), 102213.

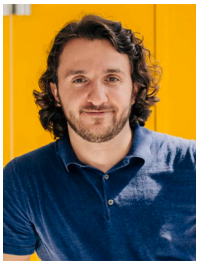

Eno Hysi received his PhD from the Department of Physics at Ryerson University and is currently a Banting and KRESCENT Fellow at St. Michael's Hospital, Division of Nephrology in Toronto. A Vanier Scholar throughout his PhD, Eno was first introduced to photoacoustic imaging during his BSc in Medical Physics. Eno developed photoacoustic imaging techniques for detecting red blood cell aggregation during his MSc in Biomedical Physics in 2012, graduating with a Gold Medal. His research has produced over 15 publications, 34 papers in conference proceedings, 2 book chapters/reviews and over 80 presentations. Throughout his studies, Eno was the recipient of numerous academic awards and scholarships including the Ontario Graduate Scholarship, NSERC's Alexander Graham Bell Canada Graduate Scholarship, the Vanier Canada Graduate Scholarship and most recently, two prestigious research fellowships. His research interests include ultrasound and photoacoustic tissue characterization for biomedical applications such as cancer treatment monitoring and blood hemodynamics as well as assessing transplant organ quality.

Muhannad N. Fadhel completed his B.Sc. Hons in Biology with biophysics minor at Ryerson university in 2011. In 2014, he earned his M.Sc. in Biomedical physics from Ryerson University with a title of "Ultra-high frequency acoustic impedance imaging of cancer cells". The research focused on understanding the source of the scattered ultrasound signals from biological structures to improve the current techniques in analyzing and quantifying ultrasound images. In 2020, he earned his PhD at Ryerson University under the supervision of Dr. Michael Kolios. Dr. Fadhel's research focuses on the use of quantitative analysis and multispectral imaging to improve the capability of photoacoustics imaging to detect physical and biochemical changes red blood cells undergo in response to cancer therapy. Currently he is starting residency in diagnostic medical physics at Yale New Haven Hospital.

Joseph A. Sebastian received his BEng degree in biomedical engineering and a minor in physics from Ryerson University, Ontario, Canada, in 2019. Currently, he is a PhD student studying shear wave elastography in organ microtissues at the University of Toronto with Dr. Craig Simmons and Dr. Michael Kolios. His research interests include high-frequency quantitative ultrasound and photoacoustics, acoustic microscopy, and tissue engineering.

Agata Exner is Professor of Radiology and Biomedical Engineering at Case Western Reserve University School of Medicine in Cleveland, Ohio. Her research focuses on development of nanobubble contrast agents for ultrasound molecular imaging and ultrasound-enhanced drug delivery for cancer detection and therapy, and engineering drug–eluting polymer implants for intratumoral chemotherapy. Dr Exner is a Fellow of the Academy of Medical and Biological Engineering, Distinguished Investigator of the Academy of Radiology Research, Ultrasound Section Editor of *Molecular Imaging and Biology* Journal and Associate Editor of the *Annals of Biomedical Engineering*. Dr. Exner is Associate Director of the Case Medical Scientsit Training Program, Chair of the Institutional Animal Care and Use Committee, recipient of the Mather Spotlight Prize for Women Faculty. Dr. Exner obtained her Ph.D. from Case Western Reserve University in 2003.

Michael C. Kolios is a Professor in the Department of Physics at Ryerson University and associate Dean of Research and Graduate Studies in the Faculty of Science. His work focuses on the use of ultrasound and optics in the biomedical sciences. He has published 140 peer-reviewed journal publications, 5 book chapters, and 190 papers in conference proceedings. He has received numerous teaching and research awards, including the American Institute of Ultrasound in Medicine Joseph H. Holmes Basic Science Pioneer Award, the Canada Research Chair in Biomedical Applications of Ultrasound and the Ontario Premier's Research Excellence Award. He is on the editorial board of the journals Ultrasound Imaging and Photoacoustics and is member of many national and international committees, including the IEEE International Ultrasonics Symposium Technical Program Committee. He regularly reviews for various funding agencies and was a charter member of the National Institutes of Health (NIH) Biomedical Imaging Technology A study section and is a member of the College of Reviewers for the Canadian Institutes of Health Research (CIHR).